








Large-area optoelectronic-grade InSe thin films via controlled phase evolution

Cite as: Appl. Phys. Rev. 7, 041402 (2020); <https://doi.org/10.1063/5.0023080>

Submitted: 26 July 2020 . Accepted: 16 October 2020 . Published Online: 02 November 2020

Hadallia Bergeron, Linda M. Guiney, Megan E. Beck, Chi Zhang,  Vinod K. Sangwan, Carlos G. Torres-Castanedo, J. Tyler Gish, Rahul Rao, Drake R. Austin, Silu Guo,  David Lam, Katherine Su,  Paul T. Brown, Nicholas R. Glavin, Benji Maruyama,  Michael J. Bedzyk,  Vinayak P. Dravid, and  Mark C. Hersam

COLLECTIONS

 This paper was selected as Featured



View Online



Export Citation



CrossMark

ARTICLES YOU MAY BE INTERESTED IN

[Featureless adaptive optimization accelerates functional electronic materials design](#)

Applied Physics Reviews 7, 041403 (2020); <https://doi.org/10.1063/5.0018811>

[Cathodoluminescence in single and multiwall WS₂ nanotubes: Evidence for quantum confinement and strain effect](#)

Applied Physics Reviews 7, 041401 (2020); <https://doi.org/10.1063/5.0019913>

[Unveiling the dimensionality effect of conductive fillers in thick battery electrodes for high-energy storage systems](#)

Applied Physics Reviews 7, 041405 (2020); <https://doi.org/10.1063/5.0024123>



Overachiever.

APR's 17.054 Journal Impact Factor makes your decision of where to publish much easier.

SUBMIT NOW!



Applied Physics Reviews

17.054
14.588
12.577



Large-area optoelectronic-grade InSe thin films via controlled phase evolution

Cite as: Appl. Phys. Rev. **7**, 041402 (2020); doi: [10.1063/5.0023080](https://doi.org/10.1063/5.0023080)

Submitted: 26 July 2020 · Accepted: 16 October 2020 ·

Published Online: 2 November 2020









View Online



Export Citation



CrossMark

Hadallia Bergeron,¹ Linda M. Guiney,¹ Megan E. Beck,¹ Chi Zhang,¹ Vinod K. Sangwan,¹ 
Carlos G. Torres-Castanedo,¹ J. Tyler Gish,¹ Rahul Rao,² Drake R. Austin,² Silu Guo,¹ David Lam,¹ 
Katherine Su,¹ Paul T. Brown,¹ 
Nicholas R. Glavin,² Benji Maruyama,² Michael J. Bedzyk,¹ 
Vinayak P. Dravid,¹ 
and Mark C. Hersam^{1,3,4,a)} 

AFFILIATIONS

¹Department of Materials Science and Engineering, Northwestern University, Evanston, Illinois 60208, USA

²US Air Force Research Laboratory, Wright-Patterson AFB, Ohio 45433-7131, USA

³Department of Chemistry, Northwestern University, Evanston, Illinois 60208, USA

⁴Department of Electrical and Computer Engineering, Northwestern University, Evanston, Illinois 60208, USA

^{a)}Author to whom correspondence should be addressed: m-hersam@northwestern.edu

ABSTRACT

Indium monoselenide (InSe) is an emerging two-dimensional semiconductor with superlative electrical and optical properties whose full potential for high-performance electronics and optoelectronics has been limited by the lack of reliable large-area thin-film synthesis methods. The difficulty in InSe synthesis lies in the complexity of the indium-selenium phase diagram and inadequate understanding of how this complexity is manifested in the growth of thin films. Herein, we present a systematic method for synthesizing InSe thin films by pulsed laser deposition followed by vacuum thermal annealing. The controlled phase evolution of the annealed InSe thin films is elucidated using a comprehensive set of *in situ* and *ex situ* characterization techniques. The annealing temperature is identified as the key parameter in controlling phase evolution with pure thin films of InSe developed within a window of 325 °C to 425 °C. To exert finer stoichiometric control over the as-deposited InSe thin film, a co-deposition scheme utilizing InSe and In₂Se₃ pulsed laser deposition targets is employed to mitigate the effects of mass loss during annealing, ultimately resulting in the synthesis of centimeter-scale, thickness-tunable ϵ -InSe thin films with high crystallinity. The optimized InSe thin films possess a strong optoelectronic response, exhibited by phototransistors with high responsivities up to 10³ A/W. Additionally, enhancement-mode InSe field-effect transistors are fabricated over large areas with device yields exceeding 90% and high on/off current modulation greater than 10⁴, realizing a degree of electronic uniformity previously unattained in InSe thin-film synthesis.

Published under license by AIP Publishing. <https://doi.org/10.1063/5.0023080>

I. INTRODUCTION

As the field of two-dimensional (2D) materials evolves from fundamental studies to applied technology, methods for achieving high-quality thin-film growth over large areas are of increasing importance. Among the 2D semiconductors, indium monoselenide (InSe) has attracted significant attention due to its superlative electronic and optical properties in addition to its bandgap tunability as a function of thickness in the ultrathin limit.^{1–3} This tunability is mediated by van der Waals interlayer coupling, which is also responsible for the indirect-to-direct bandgap transition in InSe with increasing layer thickness.⁴ Moreover, thin InSe flakes have been shown to be suitable for high-performance electronics when interfaced with metallic indium^{5,6} and with high- κ dielectrics,^{2,7} polymethyl methacrylate,⁸ or a

combination of both.⁹ As a result, InSe is being actively pursued for field-effect transistors (FETs),^{9,10} photodetectors,^{11,12} and as a platform for the study of low-dimensional physics.^{2,13,14}

Despite its desirable electronic and optical properties, InSe is a relatively under-investigated 2D semiconductor, largely because high-quality samples have only been achieved via mechanical exfoliation as opposed to large-area thin-film growth. The complex indium-selenium phase diagram¹⁵ makes synthesizing pure InSe over large areas a more difficult task than many of the extensively studied and vapor-phase synthesized van der Waals 2D materials systems that have relatively simple phase diagrams (e.g., MoS₂).¹⁶ Thus, systematic fundamental studies aimed at characterizing and understanding growth mechanisms are needed for InSe thin films. As shown in

Fig. 1(a), the indium-selenium phase diagram contains many stable phases of various stoichiometries (e.g., In_4Se_3 , InSe , In_6Se_7 , and In_2Se_3),¹⁷ and the targeted phase (InSe) only exists as a narrow line highlighted in green. In contrast, pure MoS_2 forms over a large region of the molybdenum-sulfur phase diagram (Fig. S1 in the supplementary material). Furthermore, the higher thermal stability of In_2Se_3 ¹⁸ presents a significant barrier to achieving high-quality synthesis of InSe thin films. Consequently, pure InSe nanoflakes have only been observed in a narrow parameter space for chemical vapor deposition (CVD),¹⁹ and the fine stoichiometric control necessary for reliable spatial homogeneity is lacking in powder-based CVD methods.^{20,21}

In addition to stoichiometric variation, InSe also exhibits multiple stacking polytypes including β - InSe , ε - InSe , and γ - InSe [Fig. 1(b)]. As stacking polytypes, all three structures have the same in-plane structure, which consists of a hexagonal single layer with lattice parameter $a = 4.00 \text{ \AA}$. In the out-of-plane direction, γ - InSe exhibits ABC stacking resulting in a 3R structure with $c = 25.32 \text{ \AA}$, while β - InSe and ε - InSe exhibit AB stacking resulting in a 2H structure with $c = 16.64 \text{ \AA}$.²² β - InSe differs from ε - InSe and γ - InSe in that alternating layers are rotated by 60° . As a result, β - InSe is centrosymmetric when even-layered, whereas both ε - InSe and γ - InSe are noncentrosymmetric. The noncentrosymmetric structures of ε - InSe and γ - InSe make these specific polytypes attractive for nonlinear optical applications^{23,24} such as second harmonic generation.^{19,25–28} Other thermodynamically stable polymorphs of InSe have been theoretically predicted to have even wider bandgap tunability and higher electron mobilities, offering further opportunities for enhanced electronic performance.²⁹ However, these polymorphs have yet to be observed experimentally.

Recent efforts aimed at growing InSe thin films include chemical vapor transport (CVT),^{7,30} physical vapor transport (PVT),^{25,31} chemical vapor deposition (CVD),^{19,32} molecular beam epitaxy (MBE),³³ and pulsed laser deposition (PLD).^{34,35} However, device demonstrations from these efforts have been limited to single devices rather than large-area statistical evaluation, suggesting challenges in achieving wafer-scale uniformity. Furthermore, the ambient instability of InSe ^{36,37} requires careful synthesis and device fabrication schemes that limit ambient exposure. As such, the large-area growth and device implementation of optoelectronic-grade InSe thin films remains elusive.

Herein, we employ *in situ* x-ray diffraction (XRD) and diverse surface characterization techniques to study the structural and compositional evolution of InSe thin films deposited by PLD and subsequently processed via vacuum thermal annealing. By monitoring the thin films as a function of post-deposition annealing temperatures, we systematically determined the synthesis conditions that result in ε - InSe thin films with high uniformity over large areas, controlled thickness, and no detectable impurity phases. Using this optimized deposition and post-annealing method, bottom-gated phototransistors were fabricated to explore the optoelectronic response of the InSe thin films, resulting in high responsivities up to 10^3 A/W . Finally, to demonstrate large-area device uniformity, InSe thin films were patterned into arrays of top-gated enhancement-mode FETs with device yields in excess of 90% and consistent device behavior over an area of 1 cm^2 . Ultimately, this work provides a roadmap for navigating InSe synthesis that enables the realization of large-area InSe thin films with high crystallinity, thickness tunability, and generalizability to a wide range of substrates suitable for optoelectronic applications.

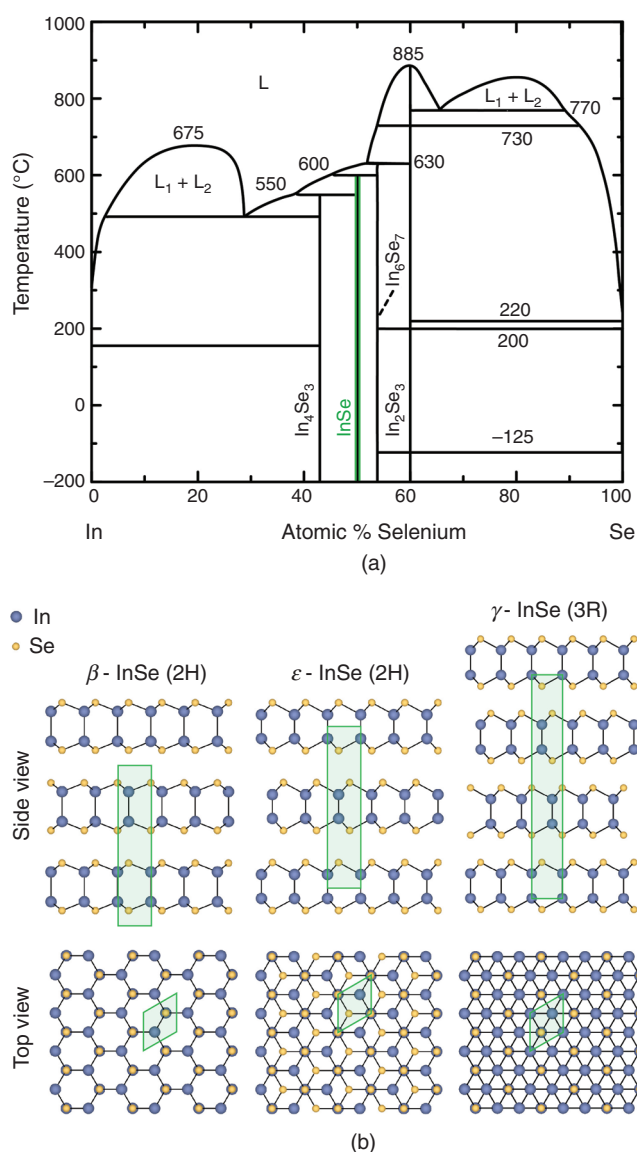


FIG. 1. Indium-selenium phase diagram and polytypes of InSe . (a) Indium-selenium phase diagram. It can be seen that the indium-selenium phase diagram contains many stable phases of various stoichiometries (e.g., In_4Se_3 , InSe , In_6Se_7 , and In_2Se_3). The InSe phase only exists as a narrow line highlighted in green. Adapted with permission from Ref. 15. (b) In addition to stoichiometric variation, InSe also exhibits multiple stacking polytypes, including β - InSe , ε - InSe , and γ - InSe , with the side and top views of the structures highlighted in this image.

II. RESULTS AND DISCUSSION

A. Pulsed laser deposition of indium selenide films

PLD is a physical vapor deposition technique in which a high-power laser pulse is incident on a solid target, ejecting a gas-phase plume of ions and atoms that condense on a substrate opposite the target. PLD enables fine control over the thickness of the deposited film via the number of laser pulses, which is important for leveraging the

thickness-dependent properties of InSe. Another considerable advantage of this growth technique is the stoichiometric ejection of material from the target.³⁸ In contrast, powder-based CVD methods suffer from stoichiometric variability that is problematic for the complex indium-selenium material system.

The starting 1 cm × 1 cm amorphous indium selenide films were deposited onto 300-nm-thick amorphous SiO₂/Si substrates at room temperature (RT) and a pressure of 10^{−7} Torr. A 248-nm KrF excimer laser was used to ablate a target consisting of pressed InSe powder using 200 mJ pulses at a frequency of 1 Hz. Further details about the deposition parameters can be found in the [supplementary material](#). Heating the substrate during the deposition process results in a significant deficiency of Se from the deposited film due to it being more volatile than In^{34,38,39} in addition to the sticking coefficient of single Se species approaching zero at substrate temperatures higher than 200 °C.⁴⁰ This effect was also observed in previous reports of MBE-grown InSe thin films where an excess of Se was needed.^{40–42} For these reasons, deposition on a substrate at RT affords greater stoichiometric control of the deposited indium selenide film given the composition of the PLD target.

B. Evolution of indium selenide films as a function of annealing conditions

The crystallization of the PLD indium selenide films via vacuum thermal annealing was monitored using *in situ* XRD. In particular, a 30-nm-thick PLD indium selenide film was heated from room temperature to 500 °C at 30 °C/min at a pressure of 10^{−4} Torr in a furnace attachment. Diffraction patterns were collected in 10 °C and 25 °C intervals. The diffraction patterns at selected transitional temperatures are shown in Fig. 2(a) (see Fig. S2 in the [supplementary material](#) for all collected data). The film began in an amorphous state with no evident diffraction peaks, excluding a low intensity peak attributed to the Si substrate at 2θ = 33°. At 250 °C, the film started to crystallize through

the appearance of a weak diffraction peak at 27.8°. While this peak is consistent with the (330) plane of In₄Se₃, as seen in previous studies on In₄Se₃ thin films,^{41,43} a robust identification of this phase requires additional information. Complementarily, *ex situ* Raman spectra [Fig. 2(b)] collected from a 30-nm-thick indium selenide film annealed to 250 °C and cooled to RT revealed the structure to be a mixture of InSe and In₄Se₃. The modes corresponding to InSe are located at 116 cm^{−1} (A₁'), 178 cm^{−1} (E'' and E'-TO), and 226 cm^{−1} (A₁'),^{44,45} while the modes at 71 cm^{−1}, 103 cm^{−1}, and 150 cm^{−1} are indicative of In₄Se₃.^{41,46} Optical microscopy of the same film annealed at 250 °C [Fig. 2(c)] shows two distinct phases, which is consistent with partial crystallization of the film into an In₄Se₃ phase.

Between 300 °C and 400 °C, a pure InSe XRD pattern was achieved as verified by comparison with standard patterns for InSe (PDF # 04-005-5113 and 04-004-6176) and other reports of synthesized InSe crystals and thin films.^{26,34,47} Specifically, the diffraction peaks at 2θ = 10.6°, 21.3°, 32.1°, and 43.3° correspond to the (002), (004), (006), and (008) planes of β-InSe and ε-InSe, or the (003), (006), (009), and (0012) planes of γ-InSe. The observation of exclusively (00*l*) diffraction peaks indicates strong texturing of the InSe crystal domains parallel to the SiO₂/Si substrate surface. This XRD pattern alone does not enable distinction between the InSe polytypes due to their similar *d*-spacing (spatial periodicity) in the out-of-plane *c*-axis direction. However, as discussed later, these crystalline InSe films can be uniquely identified as ε-InSe using electron microscopy. The corresponding *ex situ* Raman spectroscopy of a film annealed to 350 °C also shows an impurity-free spectrum consistent with InSe. In particular, the presence of the InSe A''₂ Raman mode at 200 cm^{−1} indicates the identity of the crystalline film as either γ-InSe or ε-InSe rather than β-InSe.^{48,49} Additionally, optical microscopy of the sample annealed to 350 °C shows a homogenous film [Fig. 2(d)].

Further annealing to 450 °C and above resulted in the appearance of diffraction peaks at 2θ = 26.8° and 27.3°, which is consistent with

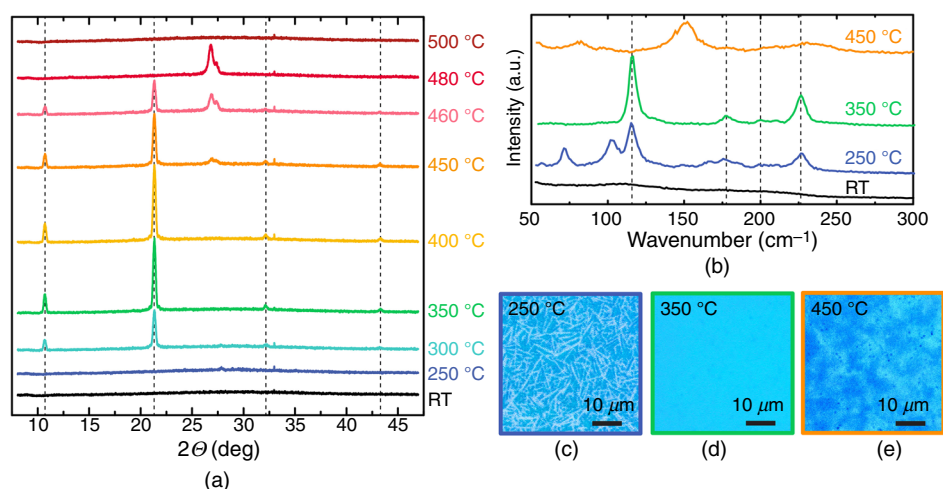


FIG. 2. Characterization of PLD indium selenide films as a function of annealing conditions. (a) *In situ* XRD of an amorphous 30-nm-thick PLD indium selenide film for different annealing temperatures between RT and 500 °C. The peaks attributed to InSe are denoted by the dashed lines. (b) *Ex situ* Raman spectra from 30-nm-thick indium selenide films after annealing to various temperatures in the XRD instrument. The peaks attributed to InSe are denoted by the dashed lines. (c-e) Optical micrographs of indium selenide films after annealing to (c) 250 °C, (d) 350 °C, and (e) 450 °C in the XRD instrument. It can be seen that optical microscopy showcases that the samples annealed at a temperature of 350 °C are homogeneous films, in contrast to (c), which showcases a partial crystallization of the film, and (e), which showcases film inhomogeneity.

previous studies on the post-annealing of In_2Se_3 thin films wherein the two peaks correspond to the (006) planes of $\kappa\text{-In}_2\text{Se}_3$ and $\gamma\text{-In}_2\text{Se}_3$, respectively, the former of which is metastable.^{50–53} An additional diffraction peak located at $2\theta = 13.2^\circ$ emerged at 490°C and matches well with the (003) plane of $\kappa\text{-In}_2\text{Se}_3$ (see Fig. S2 in the [supplementary material](#)). The *ex situ* Raman spectrum from a film annealed to 450°C and cooled to RT reveals modes at 81 cm^{-1} , 150 cm^{-1} , and 231 cm^{-1} , which correspond to $\gamma\text{-In}_2\text{Se}_3$.³¹ However, $\kappa\text{-In}_2\text{Se}_3$ exhibits similar Raman modes,⁵¹ and thus the possibility of its co-existence with $\gamma\text{-In}_2\text{Se}_3$ cannot be ruled out. The broadness of the Raman peaks [Fig. 2(b)] and the inhomogeneity of the film as observed by optical microscopy [Fig. 2(e)] indicate material loss after annealing at 450°C . At 500°C , complete material loss occurred due to sublimation. Altogether, this *in situ* XRD study reflects the complexity of the indium-selenium phase diagram and reveals how various stoichiometries (e.g., In_4Se_3 , InSe , and In_2Se_3) can be accessed using post-deposition annealing.

The results from the *in situ* XRD study were used to guide the post-annealing of indium selenide films inside the PLD chamber (i.e., *in situ* post-annealing). The annealing was performed using an infrared heating lamp immediately after deposition on 300-nm-thick SiO_2/Si at a pressure of 10^{-7} Torr. This procedure eliminates exposure of the films to ambient conditions between the deposition and annealing step. The Raman spectra at selected temperatures [Fig. 3(a)] illustrate a structural evolution in 8-nm-thick indium selenide films that closely follows the trends observed in the *in situ* XRD study (see Fig. S3 in the [supplementary material](#) for all collected Raman spectra). The onset of

crystallization occurred at 220°C , resulting in In_4Se_3 Raman modes at 71 cm^{-1} , 103 cm^{-1} , and 150 cm^{-1} . At higher temperatures, the coexistence of InSe and In_4Se_3 was observed until a threshold temperature (370°C) at which point the In_4Se_3 phase disappeared, leaving pure InSe . This threshold temperature differs by $\sim 20^\circ\text{C}$ between the PLD and XRD instruments, presumably due to the differences in the chamber pressure and heating mechanism. Annealing to 450°C resulted in the appearance of Raman modes at 110 cm^{-1} , 173 cm^{-1} , and 204 cm^{-1} , which correspond to $\beta\text{-In}_2\text{Se}_3$.^{31,54,55} Interestingly, $\beta\text{-In}_2\text{Se}_3$ was formed by post-annealing the 8-nm-thick films to high temperatures ($\geq 450^\circ\text{C}$) in the PLD instrument, whereas $\gamma\text{-In}_2\text{Se}_3$ was formed in the 30-nm-thick films in the *in situ* XRD experiment. We attribute this apparent discrepancy to the difference in the thickness of the samples, since high-temperature post-annealing of thicker films ($\sim 45\text{ nm}$) in the PLD instrument resulted in $\gamma\text{-In}_2\text{Se}_3$ (see Fig. S4 in the [supplementary material](#)). The effect of thickness on stabilizing different In_2Se_3 polymorphs has been studied recently, where previous reports have suggested that $\beta\text{-In}_2\text{Se}_3$ can only be obtained at room temperature in the 2D limit, whereas bulk $\beta\text{-In}_2\text{Se}_3$ has only been observed at high temperatures ($>200^\circ\text{C}$).^{55,56} In addition, Choi *et al.*⁵⁷ demonstrated electrically driven and reversible phase switching between $\beta\text{-In}_2\text{Se}_3$ and $\gamma\text{-In}_2\text{Se}_3$ in exfoliated flakes, attesting to the existence of transitional pathways between the two structures in ultra-thin samples.

To further study the compositional evolution of the 8-nm-thick indium selenide films, *ex situ* x-ray photoelectron spectroscopy (XPS)

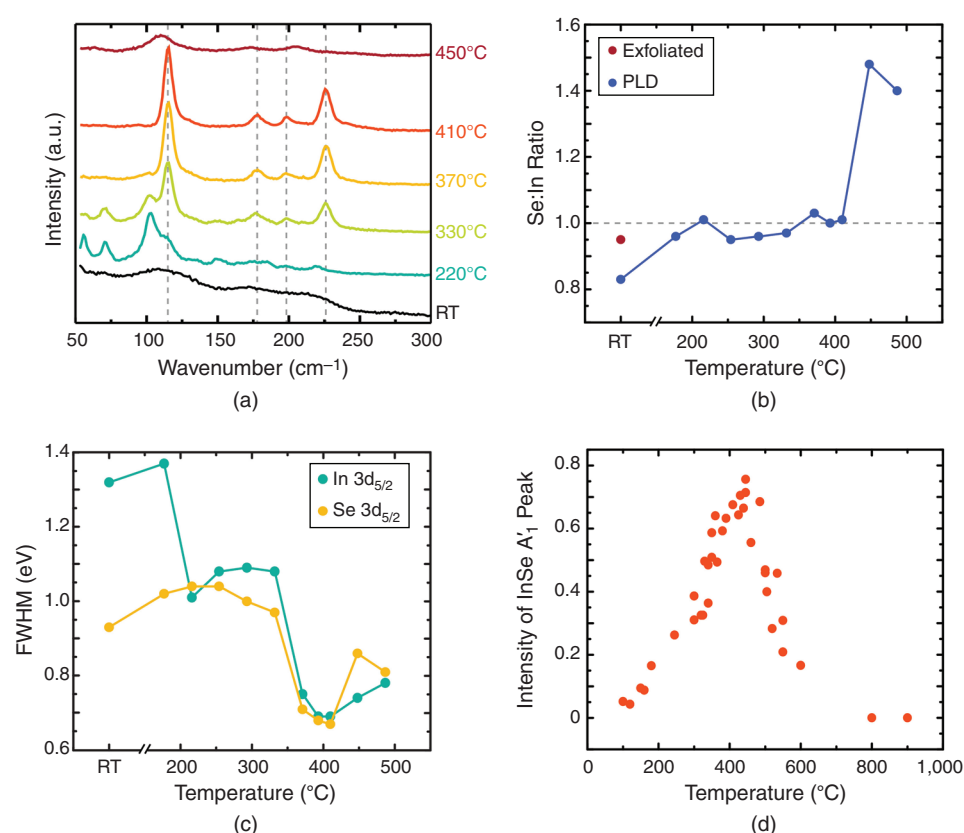


FIG. 3. Characterization of indium selenide films following post-annealing in [(a)–(c)] the PLD chamber and (d) using laser irradiation in ARES. (a) Raman spectra from 8-nm-thick indium selenide films following post-annealing at various temperatures. The annealing was performed *in situ* directly after deposition in the PLD chamber and shows a similar trend to the *in situ* XRD annealing study. The peaks attributed to InSe are denoted by dashed lines. (b) The selenium-to-indium ratio, as determined by XPS, and the (c) FWHM of the $\text{In } 3d_{5/2}$ and $\text{Se } 3d_{5/2}$ XPS peaks from 8-nm-thick indium selenide films following post-annealing at various temperatures. The targeted Se:In ratio of 1:1 for InSe is denoted by the dashed line. (d) *In situ* Raman spectroscopy results from 8-nm-thick indium selenide films on Si micro-pillars annealed using laser irradiation. The plot shows the ratio of the intensity of the $\text{InSe } A'_1$ Raman peak at $\sim 116\text{ cm}^{-1}$ to the intensity of the Si substrate Raman mode at $\sim 520\text{ cm}^{-1}$ as a function of annealing temperature. The intensity of the $\text{InSe } A'_1$ Raman peak is maximized at $\sim 400^\circ\text{C}$.

was employed. The Se:In ratios of the films following post-annealing at various temperatures are plotted in Fig. 3(b) and match well with the structural evolution studied using Raman spectroscopy. The stoichiometry of a bulk single crystal of InSe was also measured for comparison. Initially, the as-deposited PLD indium selenide film at room temperature was Se-deficient with a Se:In ratio of 0.8, likely due to the PLD plume primarily containing atomic Se species with poor sticking coefficients. However, annealing of the films resulted in stoichiometric 1:1 InSe through the relative loss of In. Further annealing to 450 °C resulted in an increase in the Se:In ratio to 1.5 corresponding to In_2Se_3 , followed by Se loss at 500 °C.

Since the vapor pressure of In is lower than both InSe and In_2Se_3 , which, in turn, have lower vapor pressures than elemental Se,⁴⁰ it is unlikely that the In loss proceeds via elemental In. Instead, previous studies showed that the evaporation products of both InSe and In_2Se_3 are In_2Se and Se_2 .^{58–60} Therefore, we conclude that the relative loss of indium in our films most likely occurs through the evaporation of In_2Se . The decrease in the Se:In ratio from 1.5 to 1.4 at 500 °C is then enabled by preferential evaporation of Se_2 from In_2Se_3 . The formation of In_2Se_3 from InSe using thermal annealing has been previously reported,^{61,62} although most reports of such phase conversions rely on variable In and Se sources with heated deposition. Additionally, we cannot preclude the possibility that the film rapidly passes through alternative stoichiometries such as In_5Se_7 or In_6Se_7 en route to In_2Se_3 from InSe. Nevertheless, the characterization of the cooled films matches well with In_4Se_3 , InSe, and In_2Se_3 at the various post-annealing temperatures.

Additional insight into the purity of the chemical coordination of the In and Se atoms was obtained from the full-width-at-half-maximum (FWHM) of the In $3d_{5/2}$ and Se $3d_{5/2}$ XPS peaks [Fig. 3(c)]. Due to the amorphous nature of the as-deposited film, the FWHM of the peaks of both elements were initially large in value (>0.9 eV), where the larger In $3d_{5/2}$ FWHM can be attributed to the relative deficiency of Se upon room temperature deposition. Upon the onset of crystallization at 220 °C, the In $3d_{5/2}$ peak sharpened, indicating a significant alignment in the chemical coordination of In that coincided with the relative loss of excess In to achieve a 1:1 Se:In ratio. This behavior is consistent with the partial crystallization of the film into In_4Se_3 as observed by Raman spectroscopy. Full minimization of the FWHM for both elemental peaks occurred between 370 °C and 410 °C, coinciding with the temperature range for pure InSe. Post-annealing to 450 °C then broadened the In $3d_{5/2}$ and Se $3d_{5/2}$ peaks again due to degradation and material loss. The FWHM of the XPS peaks were minimized for films annealed at 410 °C, reaching a minimum value of 0.7 eV for both In $3d_{5/2}$ and Se $3d_{5/2}$. For comparison, the FWHM measured for the In $3d_{5/2}$ and Se $3d_{5/2}$ peaks of bulk InSe single crystal were also 0.7 eV (Fig. S5 in the [supplementary material](#)), attesting to the purity of the synthesized films.

The generalizability of the PLD deposition and vacuum post-annealing procedure for obtaining crystalline InSe was investigated on (1) a different substrate and (2) using a different annealing method. First, we studied the crystallization of 8-nm-thick InSe films deposited on *c*-plane sapphire and post-annealed in the PLD chamber. As deduced from *ex situ* Raman spectroscopy (Fig. S6 in the [supplementary material](#)), the optimal post-annealing temperature for InSe films on *c*-plane sapphire substrates was ~ 390 °C, which agrees well with the optimal temperatures for InSe films on 300-nm-thick

SiO_2/Si obtained previously (~ 400 °C). Second, we investigated the effect of vacuum laser annealing on PLD InSe films. In this case, 8-nm-thick amorphous PLD InSe films were deposited on Si micropillars, which were then individually heated using laser irradiation in an Autonomous Research System (ARES), as described in previous reports.^{63,64} The crystallization of the InSe films was monitored using *in situ* Raman spectroscopy as each pillar was heated individually by the laser to a specified temperature and annealed for 90 s at a pressure of 10^{-4} Torr. The ratio of the intensity of the InSe A'_1 Raman peak at $\sim 116\text{ cm}^{-1}$ to the intensity of the Si substrate Raman mode at $\sim 520\text{ cm}^{-1}$ was maximized at an optimal annealing temperature of ~ 400 °C [Fig. 3(d)], corresponding well to optimal temperatures for annealing the InSe films in the PLD chamber and suggesting that these temperatures are generalizable to other annealing treatments. A representative Raman spectrum from a laser-annealed InSe film is presented in Fig. S7 in the [supplementary material](#).

C. Optimal InSe thin film synthesis conditions

From the study of the structural and compositional evolution of PLD InSe films processed using vacuum thermal annealing, it is clear that temperature is the principal parameter in the phase control of InSe films. We used this insight to guide the optimal synthesis conditions for pure InSe ultrathin films. Both the *in situ* XRD experiment and *ex situ* characterization of InSe films annealed in the PLD chamber indicated that pure InSe is formed in the temperature window of 325 °C–425 °C. Similarly, post-annealing in the PLD chamber at a temperature of ~ 400 °C yielded pure InSe. It should be noted that due to the nature of the infrared heating element, there are slight shifts in the nominal optimal annealing temperatures depending on the substrate used and the thickness of the InSe film. The compositional study also revealed a process of mass loss to achieve the targeted stoichiometry of 1:1 In:Se. While the mass loss mediates a transition to structurally and compositionally pure InSe, we also suspect that it is detrimental to the quality of the InSe film. As discussed in more detail later, reducing the stoichiometric mismatch between the starting amorphous film and the targeted 1:1 In:Se composition resulted in improved morphology and electronic properties of the annealed InSe films. Consequently, we developed a co-deposition scheme using both an InSe and In_2Se_3 PLD target to enrich the initial room-temperature deposited film with Se. In principle, this scheme should reduce the loss of material due to the mismatch between the starting and targeted stoichiometry. Several ratios of InSe: In_2Se_3 pulses were tested and a 4:1 ratio using a basis of 16:4 laser pulses was found to improve the initial stoichiometry to Se:In = 1.0 as measured by XPS (see the [supplementary material](#) for more details on the co-deposition procedure).

Using this co-deposition scheme of 16:4 InSe: In_2Se_3 pulses and *in situ* vacuum post-annealing at ~ 400 °C, pure InSe films of various thicknesses were synthesized on 300-nm-thick SiO_2/Si substrates. The film thickness, as determined using x-ray reflectivity (XRR), can be controlled by the total number of PLD laser pulses, as shown in Fig. 4(a). The thickness was determined using x-ray reflectivity (XRR). In addition, the thickness is compared with the vertical domain size of the films calculated using the Scherrer equation and the FWHM of the InSe (004) XRD peak. The XRR and XRD data and fits are presented in Fig. S8 (see the [supplementary material](#)). The vertical domain sizes were found to be 4.3 nm, 7.4 nm, 15.8 nm, and 22.1 nm, which match the 4.5 nm, 7.5 nm, 15.3 nm, and 23.4 nm

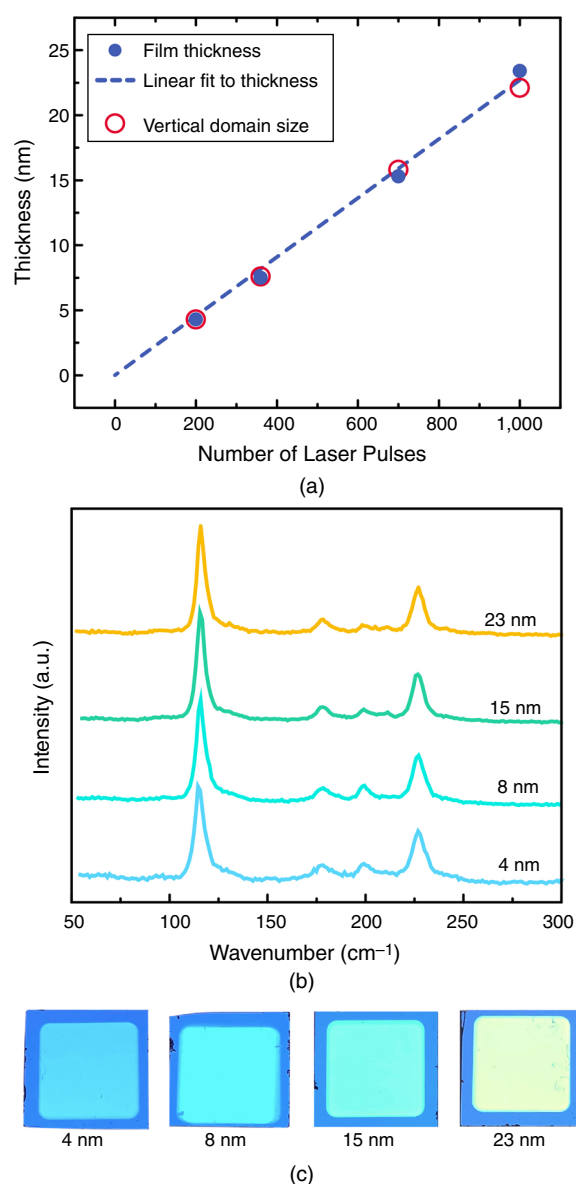


FIG. 4. Thickness tunability of the optimized PLD InSe films. The films were deposited using the 16:4 InSe:In₂Se₃ co-deposition scheme on 300-nm-thick SiO₂/Si substrates and post-annealed *in situ* at $\sim 400^\circ\text{C}$. (a) XRR and XRD determined the thickness and out-of-plane crystalline domain size, respectively, of the optimized InSe films as a function of the total number of laser pulses. A linear fit to the film thickness yields a slope of 0.2 \AA/pulse . (b) Normalized Raman spectra of films of various thicknesses showing modes corresponding to pure InSe. (c) Optical images of the optimized InSe films of various thicknesses. Here, the spectral analysis and the optical images are showing uniform, continuous, and large-area films of pure InSe ($1\text{ cm} \times 1\text{ cm}$).

thicknesses of the samples, respectively. Hence, the synthesis technique presented here yields highly (00 ℓ)-textured InSe films where the vertical domain size corresponds to the film thickness. A linear fit of the thickness of the crystallized films as a function of the number of deposition laser pulses yields an overall growth rate of 0.2 \AA/pulse .

While films thinner than the 4.5 nm film presented here can likely be obtained using this PLD method, films below 4.5 nm in thickness present considerable characterization challenges, especially for obtaining a Raman signal that allows for unambiguous identification of the InSe phase.⁴⁵ The normalized Raman spectra and optical images obtained from films of various thickness are presented in Figs. 4(b) and 4(c), respectively, showing uniform, continuous, and large-area ($1\text{ cm} \times 1\text{ cm}$) films of pure InSe.

D. Characterization of the optimized InSe thin films

Further characterization of optimized InSe films was performed to evaluate their quality. The micrometer-scale homogeneity was assessed using Raman spectroscopy mapping over a $30\text{ }\mu\text{m} \times 30\text{ }\mu\text{m}$ region of a 15-nm-thick InSe film. The position of the InSe A'₁ Raman mode over the mapped area is plotted in Fig. 5(a), showing the homogenous location of the peak at $\sim 116\text{ cm}^{-1}$. No extraneous peaks were observed, and the Raman spectra collected at each map location are plotted in Fig. S9 in the [supplementary material](#). The atomic force microscopy (AFM) height image [Fig. 5(b)] and corresponding phase image [Fig. 5(c)] of a $5\text{ }\mu\text{m} \times 5\text{ }\mu\text{m}$ area of a 15-nm-thick crystalline InSe film also show a continuous film with a root mean square (RMS) roughness of 1.0 nm. In contrast, InSe films that did not employ the InSe:In₂Se₃ co-deposition scheme exhibited an RMS roughness of 2.0 nm (Fig. S10 in the [supplementary material](#)). While films created using both deposition schemes experience the same crystallization pathway, the observed improvement in the morphology of the InSe thin films produced with the co-deposition scheme can be attributed to the reduction in mass loss and resulting reduced internal strain. The XPS spectra of the In 3d, Se 3d, and O 1s core levels of the 15-nm-thick InSe film are shown in Figs. 5(a)–5(c). From these spectra, the stoichiometry of the annealed InSe films is calculated to be identical to the initial stoichiometry of the as-deposited film (Se:In = 1.0), further supporting the absence of mass loss resulting from the co-deposition method. The peak positions of In 3d_{5/2} and In 3d_{3/2} are 445.3 eV and 452.8 eV, respectively, which match well with those of pristine exfoliated InSe in the literature,⁶⁵ as well as those of the measured bulk InSe crystal (445.3 eV and 452.9 eV). Similarly, the Se 3d_{5/2} and Se 3d_{3/2} peak positions at 54.6 eV and 55.4 eV also matched the values of pristine exfoliated InSe in the literature⁶⁵ and the bulk InSe crystal (54.7 eV and 55.5 eV). The lack of an O 1s peak confirms no detectable oxidation of the films.

The crystallinity of the optimized 15-nm-thick InSe film was investigated with scanning/transmission electron microscopy (S/TEM), selected area electron diffraction (SAED), and high-angle annular dark-field scanning transmission electron microscopy (HAADF-STEM) imaging. The sample was prepared by the direct synthesis of a 15-nm-thick InSe film on an 8-nm-thick amorphous SiO₂ support membrane for TEM and was oriented perpendicular to the [001] zone axis. Figure 6(a) shows a TEM image of the InSe film wherein the polycrystallinity of the film is apparent. From these data, we estimate lateral crystalline domain sizes of 50–150 nm. The high-resolution TEM image [Fig. 6(b)] shows a hexagonal lattice structure with d -spacing of 0.20 nm between {110} planes (denoted by the yellow lines) and 120° angle between the (100) and ($\bar{1}20$) lattice planes (denoted by the white arc), consistent with InSe. The SAED pattern along the [001] zone axis with an aperture of $\sim 110\text{ nm}$ [Fig. 6(c)] shows a single-crystal domain. The diffraction

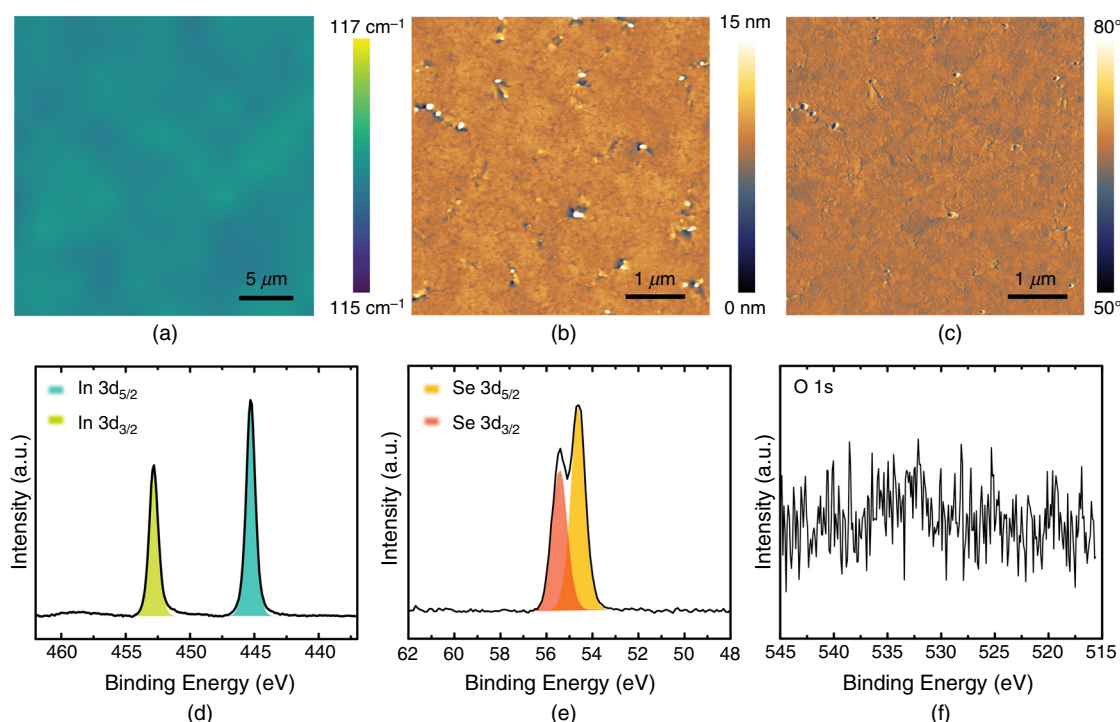


FIG. 5. Characterization of the optimized InSe films. The 15-nm-thick InSe films were synthesized using the 16:4 InSe:In₂Se₃ co-deposition scheme and *in situ* post-annealing at 410 °C. (a) 2D Raman spectroscopy map of the InSe A'₁ Raman mode peak position. The uniformity of the map shows the homogeneity of the position of the A'₁ Raman mode at ~116 cm⁻¹. No impurity peaks were detected. (b) AFM height image of an InSe film. (c) AFM phase image of the image in (b). (d) In 3d, (e) Se 3d, and (f) O 1s core-level XPS spectra of the InSe film. The lack of an O 1s peak in the spectrum confirms no detectable oxidation of the films.

spots can be indexed to the ϵ -InSe structure, as marked in the figure. The SAED pattern with a larger aperture of ~900 nm [Fig. 6(d)] reveals the polycrystallinity of the sample with all of the diffraction rings accountable to the InSe structure and also confirms the absence of impurity phases. For comparison, TEM data for an InSe film prepared using the InSe target alone is presented in Fig. S11 in the [supplementary material](#).

Due to similar in-plane structures, discerning the exact polytype of synthesized InSe thin films can prove difficult with most characterization techniques. However, HAADF-STEM paired with imaging simulations have been shown with exfoliated InSe to successfully identify the polytype.²⁶ We used this approach to identify our InSe thin films as ϵ -InSe. The experimental HAADF-STEM image obtained from the 15-nm-thick InSe film is shown in Fig. 6(e). Since contrast in HAADF strongly depends on the atomic number, the differences in intensity of the atomic columns can be used to distinguish polytypes. As illustrated in the top view of the structural schematics in Fig. 1(b), the presence of atoms at the center of the hexagonal rings rules out β -InSe, and the contrast between the intensities of the center and ring atoms suggests that the structure corresponds to ϵ -InSe rather than γ -InSe. These differences in contrast are clear in the simulated HAADF images [Fig. 6(f)] where no atom column is present at the center of the hexagonal rings for β -InSe, an atom column of equal intensity is present at the center of the hexagonal ring atoms for γ -InSe, and an atom column of significantly reduced intensity is present at the center of the hexagonal ring atoms for ϵ -InSe. The experimental HAADF image of the

synthesized 15-nm-thick InSe film most closely matches the contrast of the ϵ -InSe polytype simulated image and agrees well with a previously reported HAADF-STEM image obtained from multilayer exfoliated ϵ -InSe.²⁶ The identification of the films as the ϵ -InSe polytype is consistent with additional observations including: (1) the InSe A''₂ Raman mode at 200 cm⁻¹ is only exhibited by ϵ -InSe and γ -InSe; (2) the first reflections in SAED belonging to the InSe (100) and (010) spots are forbidden in γ -InSe, but allowed in ϵ -InSe and β -InSe. Overall, the preceding analysis agrees with previous reports of exfoliated 2D ϵ -InSe.^{26,66}

E. InSe phototransistors

Utilizing the co-deposition scheme, we explored the optoelectronic response of our optimized InSe ultrathin films. The phototransistors were fabricated by depositing 15-nm-thick InSe on 300-nm-thick SiO₂/Si substrates. The source-drain metal contacts (10 nm In and 50 nm Au) were deposited using thermal evaporation through shadow masks in a solvent-free fabrication process. The doped Si substrate served as a bottom-gate. To achieve high photodetector performance, the channel length (L) and width (W) of the phototransistors were chosen to be 7 μm and 30 μm, respectively, since the net photocurrent gain in phototransistors scales as L⁻².^{67–69} All photocurrent measurements were conducted in a vacuum (<10⁻⁵ Torr) using a laser diode emitting at 515.6 nm (additional details can be found in the [supplementary material](#)). The transfer characteristics at a drain bias of V_D = 10 V [Fig. 7(a)] reveal that the photocurrent (I_{pc})

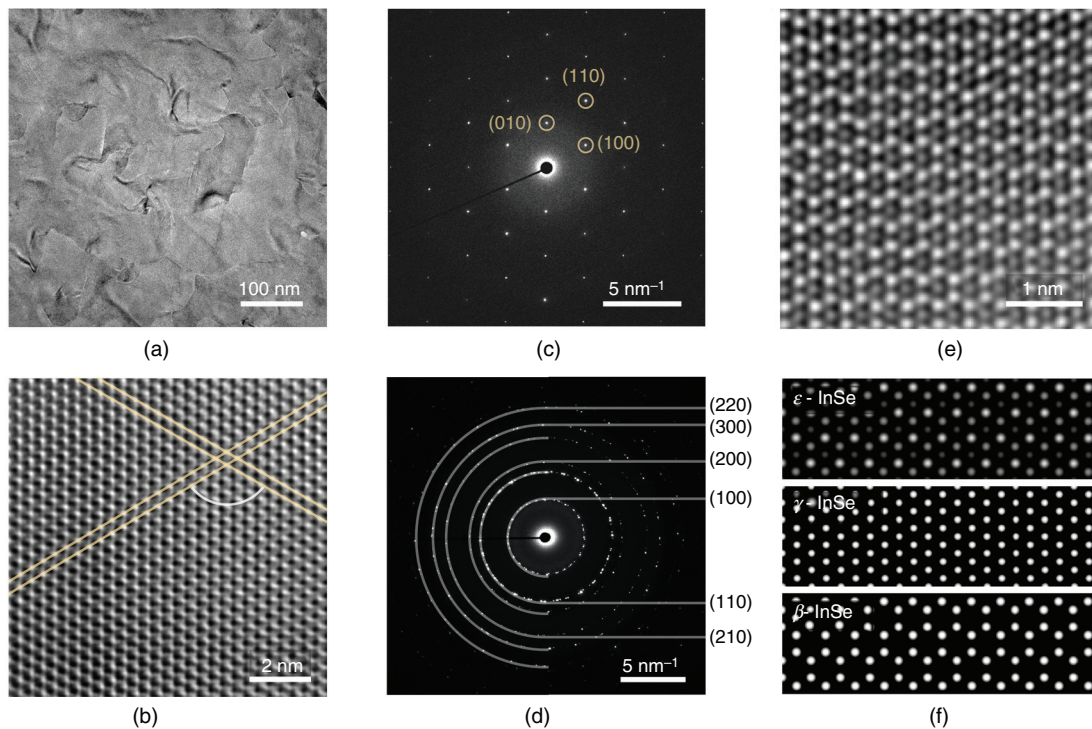


FIG. 6. TEM, SAED, and HAADF of the optimized InSe films. The 15-nm-thick InSe film was synthesized using the 16:4 InSe:In₂Se₃ co-deposition scheme and *in situ* post-annealing at 410 °C. (a) TEM image of the InSe film showing lateral grain sizes from 50 nm to 150 nm. (b) High-resolution TEM image of the InSe film along the [001] zone axis. The yellow lines denote a ~ 0.20 nm lattice spacing, and the white arc denotes a 120° angle between the (110) and (1 $\bar{2}$ 0) axes consistent with crystalline InSe. (c) SAED pattern along the [001] zone axis with a ~ 110 nm aperture showing a single crystal domain with sixfold symmetry consistent with InSe. (d) SAED pattern with a ~ 900 nm aperture showing polycrystalline InSe. (e) HAADF image of the InSe film along the [001] zone axis. (f) Simulated HAADF images for the polytypes of InSe, showing that the observed contrast in (e) best corresponds to ϵ -InSe.

increased with the bottom-gate bias (V_{BG}). The drain current under illumination (I_{light}) decreased the V_{TH} by ~ 10 V such that I_{pc} exceeded the dark current (I_{dark}) by tenfold in the off state ($V_{BG} = -60$ V), indicating an extrinsic gain mechanism of the photovoltaic effect arising from trapped charges in the channel (Fig. S12 in the [supplementary material](#)).^{68,70} The temporal photoresponse at $V_{BG} = 80$ V and $V_D = 10$ V was probed by a modulating laser, resulting in rise and fall times of 1 ms and 2.5 ms, respectively [Fig. 7(b)]. The photoconductivity mechanism was further probed by varying the illumination intensity (P). The I_{pc} measured at $V_{BG} = 80$ V and $V_D = 10$ V in three devices was found to increase with P as $P^{0.43 \pm 0.03}$, $P^{0.47 \pm 0.02}$, and $P^{0.47 \pm 0.01}$, resulting in a responsivity ($R = I_{pc}/P$) varying approximately as $R \sim P^{-0.5}$ [Figs. 7(c) and 7(d)]. This power law behavior suggests the dominance of bimolecular recombination, similar to what has been previously observed in exfoliated InSe phototransistors in accumulation.^{36,67,71} The maximum value of R obtained at low intensity ($0.1 \mu W/cm^2$) approached $\sim 10^3$ A/W, which exceeds previously reported values for phototransistors fabricated from scalable ultrathin InSe films,^{25,34} as well as thicker films of solution-processed InSe nanoflakes.^{71,72}

F. Large-area top-gated InSe FETs

We further leveraged the optimized co-deposition synthesis technique for the fabrication of enhancement-mode top-gated ultrathin

InSe FETs over large areas. Both the InSe channels and FET contacts (10 nm In and 70 nm Au) were patterned using shadow masks for a solvent-free fabrication process. The channel length and width were 100 μm and 150 μm , respectively. Following InSe:In₂Se₃ co-deposition, the patterned films were directly annealed at ~ 400 °C in the PLD instrument to prevent ambient exposure between the co-deposition and annealing steps. When amorphous InSe films are exposed to ambient conditions prior to annealing, we observe significant degradation of the electronic properties of the film (Fig. S13 in the [supplementary material](#)). This degradation results in a large increase in both the ON and OFF current that significantly compromised the I_{on}/I_{off} ratio by orders of magnitude. Following the InSe and electrode contact depositions, an encapsulation layer of 3 nm alumina and 20 nm hafnia was deposited using atomic layer deposition to prevent ambient degradation of the InSe.^{36,73} This dielectric stack was also used as the top-gate dielectric with a measured capacitance of 437.5 $\mu F/cm^2$. An optical image of patterned 15-nm-thick InSe films with source-drain contacts (prior to top-gate fabrication for clarity) is shown in Fig. 8(a). The FETs were measured in ambient conditions.

This synthesis method enabled the realization of 118 functioning top-gated InSe FETs on a 1 cm \times 1 cm substrate, which corresponds to a 91% yield. The yield was calculated excluding fabrication errors and is detailed in the [supplementary material](#). The transfer characteristics from a single top-gated FET showed a low threshold voltage of

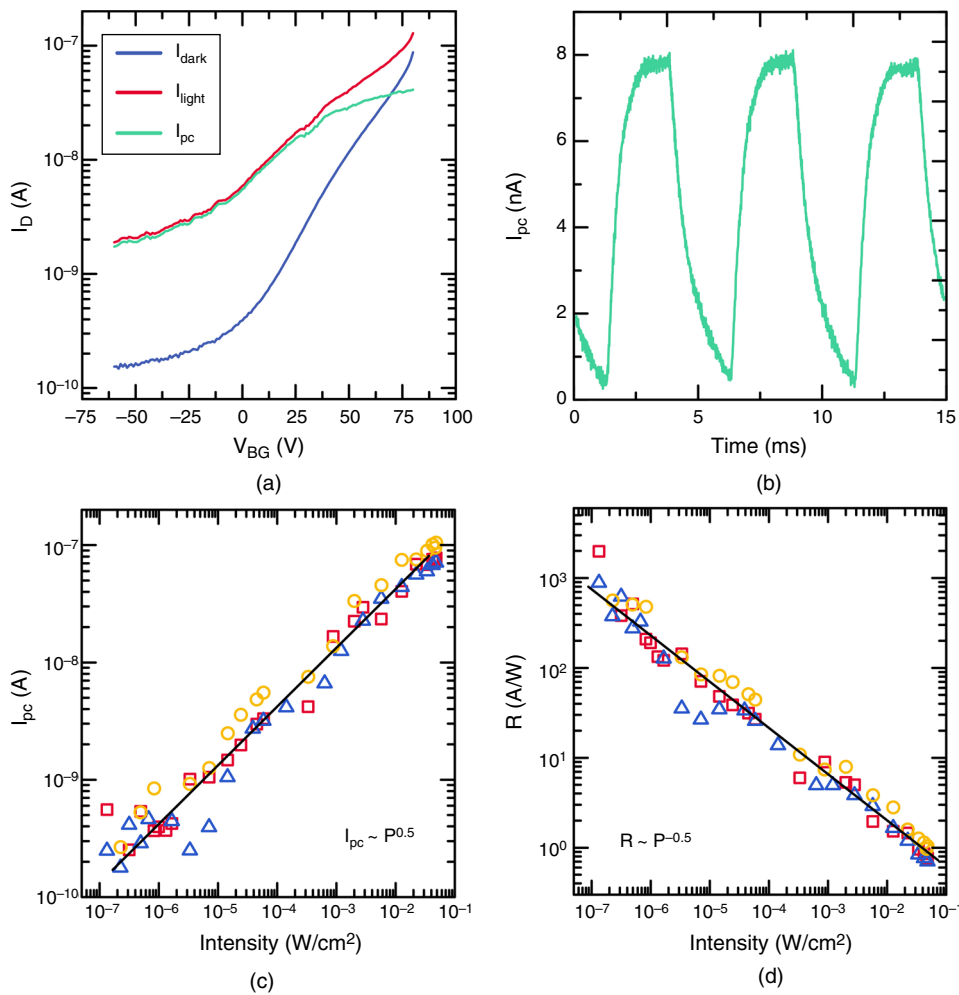


FIG. 7. Bottom-gated InSe phototransistor characteristics. The phototransistors were fabricated from 15-nm-thick InSe grown using the co-deposition scheme and post-annealing at $\sim 400^\circ\text{C}$. (a) Transfer characteristics of an InSe phototransistor with (I_{light}) and without (I_{dark}) illumination, revealing a photocurrent ($I_{\text{pc}} = I_{\text{light}} - I_{\text{dark}}$) at an illumination wavelength and intensity of 515.6 nm and 2 mW/cm^2 , respectively. The bottom-gate bias (V_{BG}) was swept from 80 to -60 V at a sweep rate of 10 V/s with V_{D} fixed at 10 V . (b) Temporal response of the InSe phototransistor obtained by switching the laser ON and OFF at a frequency of 200 Hz while the device was biased at $V_{\text{BG}} = 80\text{ V}$ and $V_{\text{D}} = 10\text{ V}$. The rise time of $\sim 1\text{ ms}$ and fall time of $\sim 2.5\text{ ms}$ was extracted from 90% of the maximum and minimum values. (c) Photocurrent vs illumination intensity (P) for three devices (yellow circles, red squares, and blue triangles) at $V_{\text{BG}} = 80\text{ V}$ and $V_{\text{D}} = 10\text{ V}$. The black line indicates $I_{\text{pc}} \sim P^{0.5}$ behavior. (d) Responsivity (R) vs intensity for the three devices, showing a maximum $R \sim 10^3\text{ A/W}$ at $0.1\text{ }\mu\text{W/cm}^2$. The black line indicates $R \sim P^{-0.5}$ behavior.

$V_{\text{TH}} = 7\text{ V}$, a high $I_{\text{on}}/I_{\text{off}}$ ratio greater than 10^4 , and a field-effect mobility of $\mu_{\text{FE}} = 0.55\text{ cm}^2\text{V}^{-1}\text{s}^{-1}$ at a source-drain bias of $V_{\text{D}} = 1\text{ V}$ [Fig. 8(b)]. The hysteresis observed is consistent with previous studies of exfoliated InSe on SiO_2 .^{6,8} A maximum $I_{\text{on}}/I_{\text{off}}$ ratio of $\sim 10^5$ was achieved when using a source-drain bias of $V_{\text{D}} = 5\text{ V}$ (Fig. S14 in the supplementary material), which is 1–2 orders of magnitude greater than previously reported FETs from 2D InSe films synthesized using scalable methods.^{25,32,34,72,74} The output characteristics of the same device as Fig. 8(b) at various top-gate voltages are shown in Fig. 8(c). At low biases ($< 0.5\text{ V}$), the output showed linear behavior, suggesting the absence of a large Schottky barrier, and the device began to saturate past $V_{\text{D}} = 1\text{ V}$. The extraction of the contact resistance would require patterning the film in Hall bars or in rectangles for the transmission line method, and the chemical reactivity of InSe precludes such lithographic patterning. The FETs demonstrated here using the InSe: In_2Se_3 co-deposition scheme showed significantly better transport properties than FETs fabricated from films using the InSe PLD target alone (see Fig. S15 in the supplementary material), which required an order of magnitude increase in source-drain voltage to attain the same $I_{\text{on}}/I_{\text{off}}$ ratio. In particular, the FETs from the InSe target alone are not

enhancement-mode and require a source-drain voltage of $V_{\text{D}} = 10\text{ V}$ to achieve an $I_{\text{on}}/I_{\text{off}}$ ratio of $\sim 10^4$, which is an order of magnitude greater V_{D} in comparison to the FETs fabricated using the InSe: In_2Se_3 co-deposition scheme. Moreover, the FETs made from the InSe: In_2Se_3 co-deposition scheme possessed over an order of magnitude greater field-effect mobility than those made from the InSe target alone. Hence, the co-deposition scheme improved both film morphology and electronic properties.

The distributions of the threshold voltage, $I_{\text{on}}/I_{\text{off}}$ ratio, and mobilities from all 118 FETs are plotted in Figs. 8(d)–8(f), respectively. The mean of the threshold voltage, $I_{\text{on}}/I_{\text{off}}$ ratio, and mobility are given by $V_{\text{TH}} = 6.8 \pm 0.2\text{ V}$, $I_{\text{on}}/I_{\text{off}} = 1.6 \pm 0.6 \times 10^4$, and $\mu_{\text{FE}} = 0.2 \pm 0.1\text{ cm}^2\text{V}^{-1}\text{s}^{-1}$, respectively. A plot of the individual transfer curves from the 118 devices is provided in Fig. S16 in the supplementary material. The tight distributions indicate consistent device behavior, and confirm that the presented synthesis method provides a scalable pathway to ultrathin InSe films for electronic applications. Furthermore, FETs from ultrathin InSe films grown using scalable vapor-phase techniques are often limited to depletion-mode operation,^{25,34} requiring an applied gate voltage to turn the

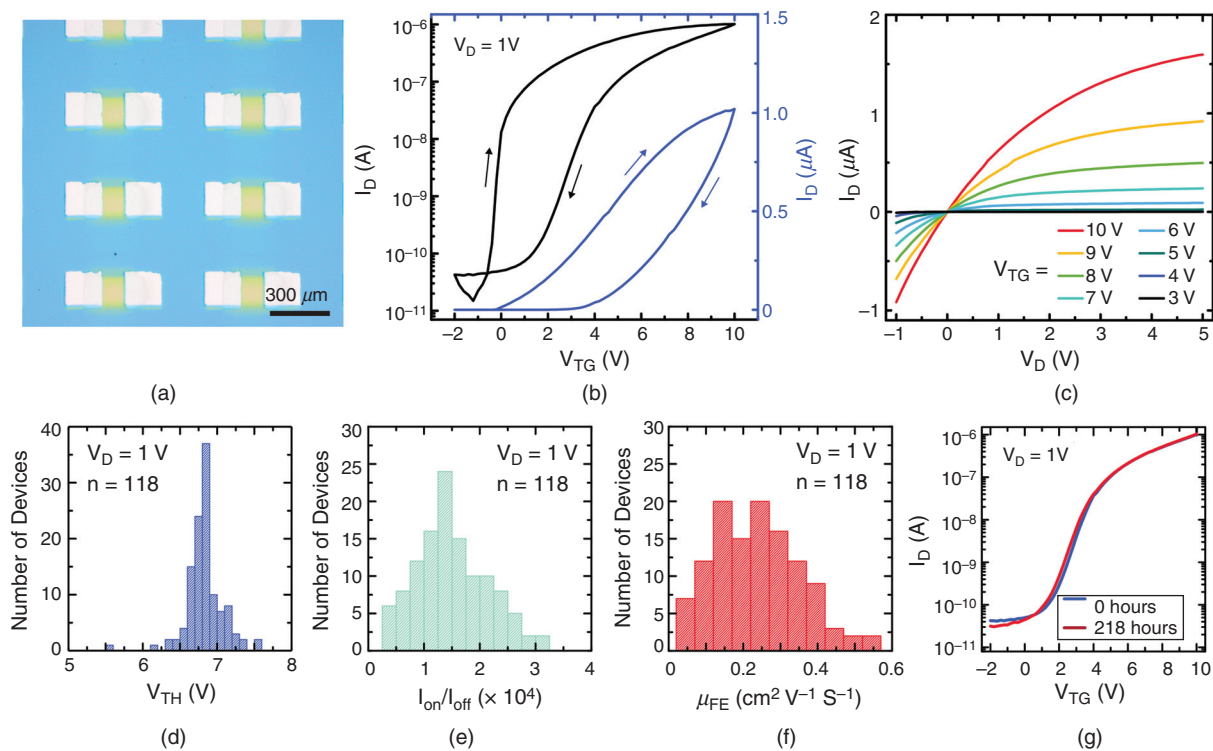


FIG. 8. Charge transport of top-gated InSe FET arrays. The FETs were fabricated from patterned 15-nm-thick InSe grown using the co-deposition scheme and post-annealing at $\sim 400^\circ\text{C}$. (a) Optical micrograph of patterned InSe channels with shadow-masked In/Au contacts prior to top-gate fabrication. (b) Transfer characteristics of an InSe top-gated FET at a source-drain bias of 1 V. (c) Output curves of the FET at various top-gate voltages. (d) Histogram of the threshold voltages (V_{TH}), (e) histogram of the $I_{\text{on}}/I_{\text{off}}$ ratios, and (f) histogram of the mobilities (μ_{FE}) of 118 top-gated FETs on a single substrate, extracted at a top-gate voltage of 10 V. The bin sizes are 0.1 V, 2500, and $0.05\text{ cm}^2\text{V}^{-1}\text{s}^{-1}$ for the threshold voltage, $I_{\text{on}}/I_{\text{off}}$ ratio, and μ_{FE} , respectively. (g) Ambient stability of the encapsulated top-gated InSe FETs, as shown by the similar transfer characteristics of the same FET immediately following fabrication and after 218 h in ambient conditions.

FET off in addition to establishing operating current levels. Notably, all of the FETs fabricated here showed enhancement-mode behavior with high complementary metal oxide semiconductor (CMOS) $I_{\text{on}}/I_{\text{off}}$ ratios of $\sim 10^4$, where I_{off} is measured at a gate voltage of 0 V. With a threshold voltage of $\sim 7\text{ V}$ and source-drain bias of 1 V, these InSe FETs demonstrate significant potential for low-power electronic devices. Finally, the encapsulated devices showed ambient stability with no change in behavior following 218 h in ambient conditions [Fig. 8(f)].

III. CONCLUSIONS

Through comprehensive characterization, this work has elucidated the structural and compositional evolution of ultrathin PLD InSe films through several phases of indium-selenium compounds as a function of the annealing temperature. In particular, *in situ* XRD of the PLD InSe films shows the progression from an amorphous film to crystalline InSe, passing through a partial In_4Se_3 crystallization and degrading into In_2Se_3 at higher temperatures. This pathway is corroborated by Raman spectroscopy and XPS measurements. Consequently, ultrathin InSe films with no detectable impurity phases can be achieved at post-deposition annealing temperatures between 325°C and 425°C . Furthermore, this study informed the development of a co-deposition scheme using both an InSe and In_2Se_3 PLD target in a

16:4 laser pulse ratio to improve the material quality by reducing stoichiometric mismatch between the starting and crystallized films. The synthesized ultrathin $\varepsilon\text{-InSe}$ films are tunable in thickness, single-crystalline in the vertical direction, and highly uniform over large areas (1 cm^2). As a result, we realized phototransistors with a responsivity of 10^3 A/W and top-gated enhancement-mode FETs with 91% yield and consistent device performance with $I_{\text{on}}/I_{\text{off}}$ ratios $> 10^4$, demonstrating a level of uniformity yet to be established for the synthesis of ultrathin InSe. This uniformity was afforded by the PLD technique that provides homogenous deposition and stoichiometric tuning of the starting material. Together with *in situ* post-annealing, the method presented here enables the controllable navigation of the complex indium-selenium phase diagram and is generalizable to a wide range of substrates suitable for nanoelectronic applications. Moreover, we anticipate that this study will serve as a roadmap to guide future efforts to synthesize large-area thin films of other layered post-transition metal chalcogenides.

SUPPLEMENTARY MATERIAL

See the [supplementary material](#) for experimental details on the deposition, *in situ* annealing, laser annealing, XRD, XRR, Raman spectroscopy, XPS, AFM, S/TEM, and FET; phototransistor fabrication and characterization; and Figs. S1–S15.

AUTHORS' CONTRIBUTIONS

H.B. and L.M.G. contributed equally to this work.

ACKNOWLEDGMENTS

This research was supported by the Materials Research Science and Engineering Center (MRSEC) of Northwestern University (NSF DMR-1720139) and the Air Force Research Laboratory under Agreement No. FA8650-15-2-5518. H.B. acknowledges support from the NSERC Postgraduate Scholarship-Doctoral Program. M.E.B. and H.B. acknowledge support from the National Science Foundation Graduate Research Fellowship Program. R.R. and B.M. acknowledge funding from the Air Force Office of Scientific Research (LRIR No. 16RXCOR322). This work made use of the Pulsed Laser Deposition Shared Facility and the Jerome B. Cohen X-Ray Diffraction Facility at the Materials Research Center at Northwestern University, which is supported by the National Science Foundation MRSEC program (DMR-1720139) and the Soft and Hybrid Nanotechnology Experimental (SHyNE) Resource (NSF ECCS-1542205). This work also made use of the EPIC and Keck-II facility of Northwestern University's NUANCE Center, which has received support from the SHyNE Resource, the MRSEC program, the International Institute for Nanotechnology (IIN), the Keck Foundation, and the State of Illinois. H.B. acknowledges Dr. D. Bruce Buchholz, Elise Goldfine, and Dr. Bernard Beckerman for their technical contributions and helpful discussions. The U.S. government is authorized to reproduce and distribute reprints for governmental purposes notwithstanding any copyright notation thereon. The views and conclusions contained herein are those of the authors and should not be interpreted as necessarily representing the official policies or endorsements, either expressed or implied, of the sponsors.

DATA AVAILABILITY

Data affiliated with this manuscript is available upon request from the corresponding author.

REFERENCES

- ¹G. W. Mudd, S. A. Svatek, T. Ren, A. Patané, O. Makarovskiy, L. Eaves, P. H. Beton, Z. D. Kovalyuk, G. V. Lashkarev, Z. R. Kudrynskiy, and A. I. Dmitriev, *Adv. Mater.* **25**, 5714 (2013).
- ²D. A. Bandurin, A. V. Tyurnina, G. L. Yu, A. Mishchenko, V. Zolyomi, S. V. Morozov, R. K. Kumar, R. V. Gorbachev, Z. R. Kudrynskiy, S. Pezzini, Z. D. Kovalyuk, U. Zeitler, K. S. Novoselov, A. Patané, L. Eaves, I. V. Grigorieva, V. I. Fal'ko, A. K. Geim, and Y. Cao, *Nat. Nanotech.* **12**, 223 (2017).
- ³C. Song, F. Fan, N. Xuan, S. Huang, G. Zhang, C. Wang, Z. Sun, H. Wu, and H. Yan, *ACS Appl. Mater. Interfaces* **10**, 3994 (2018).
- ⁴Y. Sun, S. Luo, X.-G. Zhao, K. Biswas, S.-L. Li, and L. Zhang, *Nanoscale* **10**, 7991 (2018).
- ⁵Y.-T. Huang, Y.-H. Chen, Y.-J. Ho, S.-W. Huang, Y.-R. Chang, K. Watanabe, T. Taniguchi, H.-C. Chiu, C.-T. Liang, R. Sankar, F.-C. Chou, C.-W. Chen, and W.-H. Wang, *ACS Appl. Mater. Interfaces* **10**, 33450 (2018).
- ⁶M. Li, C.-Y. Lin, S.-H. Yang, Y.-M. Chang, J.-K. Chang, F.-S. Yang, C. Zhong, W.-B. Jian, C.-H. Lien, C.-H. Ho, H.-J. Liu, R. Huang, W. Li, Y.-F. Lin, and J. Chu, *Adv. Mater.* **30**, 1803690 (2018).
- ⁷K. Yuan, R. Yin, X. Li, Y. Han, M. Wu, S. Chen, S. Liu, X. Xu, K. Watanabe, T. Taniguchi, D. A. Muller, J. Shi, P. Gao, X. Wu, Y. Ye, and L. Dai, *Adv. Funct. Mater.* **29**, 1904032 (2019).
- ⁸S. Sucharitakul, N. J. Goble, U. R. Kumar, R. Sankar, Z. A. Bogorad, F.-C. Chou, Y.-T. Chen, and X. P. A. Gao, *Nano Lett.* **15**, 3815 (2015).
- ⁹W. Feng, W. Zheng, W. Cao, and P. Hu, *Adv. Mater.* **26**, 6587 (2014).
- ¹⁰J. Jiang, J. Li, Y. Li, J. Duan, L. Li, Y. Tian, Z. Zong, H. Zheng, X. Feng, Q. Li, H. Liu, Y. Zhang, T.-L. Ren, and L. Han, *Npj 2D Mater. Appl.* **3**, 29 (2019).
- ¹¹S. R. Tamalampudi, Y.-Y. Lu, R. Kumar U, R. Sankar, C.-D. Liao, K. Moorthy B, C.-H. Cheng, F. C. Chou, and Y.-T. Chen, *Nano Lett.* **14**, 2800 (2014).
- ¹²M. Dai, H. Chen, R. Feng, W. Feng, Y. Hu, H. Yang, G. Liu, X. Chen, J. Zhang, C.-Y. Xu, and P. Hu, *ACS Nano* **12**, 8739 (2018).
- ¹³M. Hamer, E. Tóvári, M. Zhu, M. D. Thompson, A. Mayorov, J. Prance, Y. Lee, R. P. Haley, Z. R. Kudrynskiy, A. Patané, D. Terry, Z. D. Kovalyuk, K. Ensslin, A. V. Kretinin, A. Geim, and R. Gorbachev, *Nano Lett.* **18**, 3950 (2018).
- ¹⁴V. K. Sangwan and M. C. Hersam, *Annu. Rev. Phys. Chem.* **69**, 299 (2018).
- ¹⁵H. Okamoto, *J. Phase Equilibria Diffusion* **25**, 201 (2004).
- ¹⁶T. B. Massalski, *Binary Alloy Phase Diagrams*, 2nd ed. (ASM International, 1990).
- ¹⁷T. Gödecke, T. Haalboom, and F. Sommer, *J. Phase Equilibria* **19**, 572 (1998).
- ¹⁸M. Yudasaka and K. Nakanishi, *Thin Solid Films* **156**, 145 (1988).
- ¹⁹W. Huang, L. Gan, H. Li, Y. Ma, and T. Zhai, *Chem. Eur. J.* **24**, 15678 (2018).
- ²⁰S. Li, Y.-C. Lin, X.-Y. Liu, Z. Hu, J. Wu, H. Nakajima, S. Liu, T. Okazaki, W. Chen, T. Minari, Y. Sakuma, K. Tsukagoshi, K. Suenaga, T. Taniguchi, and M. Osada, *Nanoscale* **11**, 16122 (2019).
- ²¹S. Wang, Y. Rong, Y. Fan, M. Pacios, H. Bhaskaran, K. He, and J. H. Warner, *Chem. Mater.* **26**, 6371 (2014).
- ²²C. D. Blasi, G. Micocci, S. Mongelli, and A. Tepore, *J. Cryst. Growth* **57**, 482 (1982).
- ²³A. Autere, H. Jussila, Y. Dai, Y. Wang, H. Lipsanen, and Z. Sun, *Adv. Mater.* **30**, 1705963 (2018).
- ²⁴W. Yang, N. Xu, and H. Zhang, *Laser Phys. Lett.* **15**, 105101 (2018).
- ²⁵J. Zhou, J. Shi, Q. Zeng, Y. Chen, L. Niu, F. Liu, T. Yu, K. Suenaga, X. Liu, J. Lin, and Z. Liu, *2D Mater.* **5**, 025019 (2018).
- ²⁶Q. Hao, H. Yi, H. Su, B. Wei, Z. Wang, Z. Lao, Y. Chai, Z. Wang, C. Jin, J. Dai, and W. Zhang, *Nano Lett.* **19**, 2634 (2019).
- ²⁷C. Attacalite, M. Palummo, E. Cannuccia, and M. Grüning, *Phys. Rev. Mater.* **3**, 074003 (2019).
- ²⁸N. Leisgang, J. G. Roch, G. Froehlicher, M. Hamer, D. Terry, R. Gorbachev, and R. J. Warburton, *AIP Adv.* **8**, 105120 (2018).
- ²⁹Y. Sun, Y. Li, T. Li, K. Biswas, A. Patané, and L. Zhang, *Adv. Funct. Mater.* **30**, 2001920 (2020).
- ³⁰Y. Hu, W. Feng, M. Dai, H. Yang, X. Chen, G. Liu, S. Zhang, and P. Hu, *Semicond. Sci. Technol.* **33**, 125002 (2018).
- ³¹N. Balakrishnan, E. D. Steer, E. F. Smith, Z. R. Kudrynskiy, Z. D. Kovalyuk, L. Eaves, A. Patané, and P. H. Beton, *2D Mater.* **5**, 035026 (2018).
- ³²H.-C. Chang, C.-L. Tu, K.-I. Lin, J. Pu, T. Takenobu, C.-N. Hsiao, and C.-H. Chen, *Small* **14**, 1802351 (2018).
- ³³I. A. Kibirev, A. V. Matetskii, A. V. Zotov, and A. A. Saranin, *Appl. Phys. Lett.* **112**, 191602 (2018).
- ³⁴Z. Yang, W. Jie, C.-H. Mak, S. Lin, H. Lin, X. Yang, F. Yan, S. P. Lau, and J. Hao, *ACS Nano* **11**, 4225 (2017).
- ³⁵D. Zheng, J. Shiogai, K. Fujiwara, and A. Tsukazaki, *Appl. Phys. Lett.* **113**, 253501 (2018).
- ³⁶S. A. Wells, A. Henning, J. T. Gish, V. K. Sangwan, L. J. Lauhon, and M. C. Hersam, *Nano Lett.* **18**, 7876 (2018).
- ³⁷L. Shi, Q. Zhou, Y. Zhao, Y. Ouyang, C. Ling, Q. Li, and J. Wang, *J. Phys. Chem. Lett.* **8**, 4368 (2017).
- ³⁸H. M. Christen and G. Eres, *J. Phys.: Condens. Matter* **20**, 264005 (2008).
- ³⁹C. Viswanathan, V. Senthikumar, R. Sriranjini, D. Mangalaraj, S. K. Narayandass, and J. Yi, *Cryst. Res. Technol.* **40**, 658 (2005).
- ⁴⁰L. Brahim-Otsmane and J. Y. Emery, *Thin Solid Films* **237**, 291 (1994).
- ⁴¹J. Y. Emery, L. Brahim-Otsmane, M. Jouanne, C. Julien, and M. Balkanski, *Mater. Sci. Eng.: B* **3**, 13 (1989).
- ⁴²S. E. Monkad, M. Eddrief, J. P. Lacharme, K. Amimer, and C. A. Sébenne, *Surf. Sci.* **352–354**, 833 (1996).
- ⁴³N. Benramdane and R. H. Misho, *Sol. Energy Mater. Sol. Cells* **37**, 367 (1995).
- ⁴⁴S. Jandl and C. Carlone, *Solid State Communications* **25**, 5 (1978).
- ⁴⁵S. Lei, L. Ge, S. Najmaei, A. George, R. Kappera, J. Lou, M. Chhowalla, H. Yamaguchi, G. Gupta, R. Vajtai, A. D. Mohite, and P. M. Ajayan, *ACS Nano* **8**, 1263 (2014).

- ⁴⁶C. Julien, A. Khelifa, N. Benramdane, and J. P. Guesdon, *Mater. Sci. Eng.: B* **27**, 53 (1994).
- ⁴⁷A. Hirohata, J. S. Moodera, and G. P. Berera, *Thin Solid Films* **510**, 247 (2006).
- ⁴⁸C. Carlone and S. Jandl, *Solid State Communications* **29**, 31 (1979).
- ⁴⁹N. Kuroda and Y. Nishina, *Solid State Commun.* **28**, 439 (1978).
- ⁵⁰A. Chaiken, K. Nauka, G. A. Gibson, H. Lee, C. C. Yang, J. Wu, J. W. Ager, K. M. Yu, and W. Walukiewicz, *J. Appl. Phys.* **94**, 2390 (2003).
- ⁵¹C. H. de Groot and J. S. Moodera, *J. Appl. Phys.* **89**, 4336 (2001).
- ⁵²J. Jasinski, W. Swider, J. Washburn, Z. Liliental-Weber, A. Chaiken, K. Nauka, G. A. Gibson, and C. C. Yang, *Appl. Phys. Lett.* **81**, 4356 (2002).
- ⁵³Y. Yan, S. Li, Y. Ou, Y. Ji, Z. Yu, L. Liu, C. Yan, Y. Zhang, and Y. Zhao, *Electron. Mater. Lett.* **10**, 1093 (2014).
- ⁵⁴L. Liu, J. Dong, J. Huang, A. Nie, K. Zhai, J. Xiang, B. Wang, F. Wen, C. Mu, Z. Zhao, Y. Gong, Y. Tian, and Z. Liu, *Chem. Mater.* **31**, 10143 (2019).
- ⁵⁵X. Tao and Y. Gu, *Nano Lett.* **13**, 3501 (2013).
- ⁵⁶W. Feng, F. Gao, Y. Hu, M. Dai, H. Liu, L. Wang, and P. Hu, *ACS Appl. Mater. Interfaces* **10**, 27584 (2018).
- ⁵⁷M. S. Choi, B. Cheong, C. H. Ra, S. Lee, J.-H. Bae, S. Lee, G.-D. Lee, C.-W. Yang, J. Hone, and W. J. Yoo, *Adv. Mater.* **29**, 1703568 (2017).
- ⁵⁸R. Colin and J. Drowart, *Trans. Faraday Soc.* **64**, 2611 (1968).
- ⁵⁹R. S. Srinivasa and J. G. Edwards, *J. Electrochem. Soc.* **134**, 1811 (1987).
- ⁶⁰A. Chevy, A. Kuhn, and M.-S. Martin, *J. Cryst. Growth* **38**, 118 (1977).
- ⁶¹M. Osman, Y. Huang, W. Feng, G. Liu, Y. Qiu, and P. Hu, *RSC Adv.* **6**, 70452 (2016).
- ⁶²K. Lu, M. L. Sui, J. H. Perepezko, and B. Lanning, *J. Mater. Res.* **14**, 771 (1999).
- ⁶³R. Rao, A. E. Islam, P. M. Campbell, E. M. Vogel, and B. Maruyama, *2D Mater.* **4**, 025058 (2017).
- ⁶⁴R. A. Vilá, R. Rao, C. Muratore, E. Bianco, J. A. Robinson, B. Maruyama, and N. R. Glavin, *2D Mater.* **5**, 011009 (2017).
- ⁶⁵P.-H. Ho, Y.-R. Chang, Y.-C. Chu, M.-K. Li, C.-A. Tsai, W.-H. Wang, C.-H. Ho, C.-W. Chen, and P.-W. Chiu, *ACS Nano* **11**, 7362 (2017).
- ⁶⁶Z. Chen, J. Biscaras, and A. Shukla, *Nanoscale* **7**, 5981 (2015).
- ⁶⁷R. H. Bube, *Photoelectronic Properties of Semiconductors* (Cambridge University Press, 1992).
- ⁶⁸M. M. Furchi, D. K. Polyushkin, A. Pospischil, and T. Mueller, *Nano Lett.* **14**, 6165 (2014).
- ⁶⁹J. Kang, V. K. Sangwan, H.-S. Lee, X. Liu, and M. C. Hersam, *ACS Photonics* **5**, 3996 (2018).
- ⁷⁰D. Kufer and G. Konstantatos, *Nano Lett.* **15**, 7307 (2015).
- ⁷¹J. Kang, S. A. Wells, V. K. Sangwan, D. Lam, X. Liu, J. Luxa, Z. Sofer, and M. C. Hersam, *Adv. Mater.* **30**, 1802990 (2018).
- ⁷²N. Curreli, M. Serri, D. Spirito, E. Lago, E. Petroni, B. Martín-García, A. Politano, B. Gürbulak, S. Duman, R. Krahne, V. Pellegrini, and F. Bonaccorso, *Adv. Funct. Mater.* **30**, 1908427 (2020).
- ⁷³J. D. Wood, S. A. Wells, D. Jariwala, K.-S. Chen, E. Cho, V. K. Sangwan, X. Liu, L. J. Lauhon, T. J. Marks, and M. C. Hersam, *Nano Lett.* **14**, 6964 (2014).
- ⁷⁴J. Lauth, F. E. S. Gorris, M. Samadi Khoshkhoo, T. Chassé, W. Friedrich, V. Lebedeva, A. Meyer, C. Klinke, A. Kornowski, M. Scheele, and H. Weller, *Chem. Mater.* **28**, 1728 (2016).